Gyrokinetic Theory and Simulation of Zonal Flows and Turbulence in Helical Systems

T.-H.Watanabe and H.Sugama

National Institute for Fusion Science / The Graduate University for Advanced Studies,
Toki, Gifu, 509-5292, Japan

e-mail contact of main author: watanabe.tomohiko@nifs.ac.jp

Abstract. Gyrokinetic theory and simulations on ion heat transport physics in helical systems have recently been developed. Damping processes of zonal flows driven by ion temperature gradient (ITG) turbulence in helical systems have been analytically investigated based on the gyrokinetic theory as a generalization of the previous work by Rosenbluth and Hinton for tokamaks. A collisionless response function of the zonal flow to given source terms is derived by taking account of the helical geometry and finite-orbit-width effects. Validity of the analytical predictions are verified by the Eulerian gyrokinetic code (GKV code) with very-high resolution of the phase space. The GKV simulation extended to take account of helical-ripple-trapped particles is also applied to the ITG turbulence in helical systems. The ITG turbulent transport level in a model case for the inward-shifted magnetic-axis configuration with a stronger instability drive is effectively suppressed by the zonal flow, and is reduced to a level comparable to that in the less unstable case for the standard configuration with smaller side-band helical field components.

1. Introduction

Gyrokinetic theory and simulation of plasma turbulence have advanced physical understandings on the anomalous transport mechanism in magnetic confinement fusion. The ion temperature gradient (ITG) turbulence [1] and the zonal flows [2] have been intensively investigated because of their importance in considering the anomalous ion heat transport. Detailed studies on the zonal flow dynamics as well as their interactions with the ITG turbulence deepen understandings of the plasma transport mechanism. Among them, Rosenbluth and Hinton [3] have developed the theory on the zonal flow driven by the ITG turbulence in tokamaks, and have shown that in collisionless processes a zonal flow with finite amplitude remains constant after Landau damping of the geodesic acoustic mode (GAM) oscillations [4]. It is demonstrated by the gyrokinetic-Vlasov (GKV) simulation [5] that the damping process of the zonal flow and GAM is closely related to fine oscillatory velocity-space structures of the perturbed ion gyrocenter distribution function, δf. Also, a coherent structure of δf associated with the residual zonal flow is clearly identified in the GKV simulation.

The gyrokinetic theory on the zonal flow and GAM driven by the ITG turbulence is recently extended to helical systems by Sugama and Watanabe [6, 7] as a generalization of the work by Rosenbluth and Hinton for tokamaks. It turns out that helical ripples in the equilibrium field cause stronger damping of GAM than the toroidal magnetic variation does, and that drift motions of toroidally- and helically-trapped particles play a crucial role in determining the residual zonal flow amplitude. Analytical predictions about geometrical effects on GAM dispersion relation, the residual zonal flows, and the velocity-space structure of the distribution function are also verified by GKV simulations with very-high resolution of the phase space.

The gyrokinetic-Vlasov simulation by means of the GKV code has confirmed the statistically steady state of the tokamak ITG turbulent transport in terms of detailed calculation of the entropy balance [5, 8, 9] where fine velocity-space structures of δf generated in the turbulence are resolved accurately. The GKV code is also applied to a full toroidal angle simulation of the tokamak ITG turbulence by utilizing the Earth Simulator [10]. In order to elucidate how the helical geometry can be optimized to enhance the residual zonal flow level and accordingly

reduce the anomalous transport, the GKV simulation is extended to take account of helically-trapped particles, and is applied to the ITG turbulence in helical systems, which is realized by the tera-flops and tera-bytes scale computation on the Earth Simulator.

This paper is organized as follows. The theoretical and numerical models for the ITG turbulence and the zonal flow are described in the next section. Recent progress in our studies on the zonal flow and GAM is reported in section 3. In section 4, shown are results of the nonlinear GKV simulation for the ITG turbulent transport in helical systems. A summary is given in the last section.

2. Theoretical and Numerical Models

Let us consider the nonlinear gyrokinetic equation [11] for the perturbed ion distribution function, δf, in the low-β electrostatic limit. With the assumption of a large-aspect-ratio torus, the governing equation for δf is represented as

$$\begin{aligned} \frac{\partial \delta f}{\partial t} + v_\parallel \boldsymbol{b}\cdot\nabla\delta f + \frac{c}{B_0}\{\Phi,\delta f\} + \boldsymbol{v}_d\cdot\nabla\delta f - \mu\,(\boldsymbol{b}\cdot\nabla\Omega_i)\frac{\partial \delta f}{\partial v_\parallel} \\ = \left(\boldsymbol{v}_* - \boldsymbol{v}_d - v_\parallel\boldsymbol{b}\right)\cdot\frac{e\nabla\Phi}{T_i}F_M + C(\delta f) \end{aligned} \tag{1}$$

where the parallel velocity, $v_\parallel$, and the magnetic moment, μ, are chosen as the velocity-space coordinates. The Maxwellian distribution is denoted by F_M. We have employed the collision term, $C(\delta f)$, where the Lenard-Bernstein model collision operator is introduced, such that,

$$C(\delta f) = \nu_{ii}\left[\frac{1}{v_\perp}\frac{\partial}{\partial v_\perp}\left(v_\perp\frac{\partial \delta f}{\partial v_\perp} + \frac{v_\perp^2}{v_{ti}^2}\delta f\right) + \frac{\partial}{\partial v_\parallel}\left(\frac{\partial \delta f}{\partial v_\parallel} + \frac{v_\parallel}{v_{ti}^2}\delta f\right)\right], \tag{2}$$

where ν_{ii} denotes the ion-ion collision frequency. See Ref. [5] for more details, while standard notations are used in Eq.(1).

In the GKV code, we employ the toroidal flux tube model [12] with the field-aligned coordinates of $x = r - r_0$, $y = \frac{r_0}{q_0}[q(r)\theta - \zeta]$, and $z = \theta$, and also assume constant volume-averaged density and temperature gradients with scale-lengths of L_n and L_T as well as the constant magnetic shear parameter, $\hat{s}$. The averaged minor radius, r_0, is defined by $\Psi_t = \pi B_0 r_0^2$ where Ψ_t means the toroidal flux. Here, $q(r)$ stands for the safety factor, and $q_0 = q(r_0)$. The toroidal and helical effects of the confinement field are introduced by the change of magnetic field strength,

$$B = B_0\left\{1 - \varepsilon_{00}(r) - \varepsilon_t(r)\cos z - \sum_{l=L-1}^{l=L+1}\varepsilon_l(r)\cos[(l - Mq_0)z - M\alpha]\right\}, \tag{3}$$

where L and M denote the poloidal and toroidal periodicities of the helical field. For the Large Helical Device (LHD), $L = 2$ and $M = 10$. The averaged normal curvature is introduced through $\varepsilon'_{00} = d\varepsilon_{00}/dr$ [13]. The parameters representing the toroidicity and helicity are assumed to be small such that $\varepsilon_t = r_0/R_0 \ll 1$ and $|\varepsilon_l| \ll 1$, respectively, where R_0 means the major radius. Major side band helical components are considered as ε_{L-1} and ε_{L+1}. The absolute values of ε_{L-1} and ε_{L+1} become large when the magnetic axis is shifted from the standard position by changing the vertical field. We also set the field-line label α to be constant ($\alpha = 0$) because the local analysis of the linear ITG instability in helical systems shows the weak dependence on α [14].

In Eq.(1), the magnetic and diamagnetic drift terms are given as

$$\boldsymbol{v}_d\cdot\nabla = -\frac{v_\parallel^2+\Omega_i\mu}{\Omega_{i0}R_0}\left\{\left[R_0\varepsilon_{00}'+\cos z+\sum_{l=L-1}^{l=L+1}(\varepsilon_l/\varepsilon_t)l\cos\left((l-Mq_0)z-M\alpha\right)\right]\frac{\partial}{\partial y}\right. \\ \left.+\left[\sin z+\sum_{l=L-1}^{l=L+1}(\varepsilon_l/\varepsilon_t)l\sin\left((l-Mq_0)z-M\alpha\right)\right]\left(\frac{\partial}{\partial x}+\hat{s}z\frac{\partial}{\partial y}\right)\right\}, \tag{4}$$

$$\boldsymbol{v}_*\cdot\nabla = -\frac{cT_i}{eL_nB_0}\left[1+\eta_i\left(\frac{m_iv^2}{2T_i}-\frac{3}{2}\right)\right]\frac{\partial}{\partial y}\,. \tag{5}$$

Here, $\Omega_{i0}=eB_0/m_ic$, $\eta_i=L_n/L_T$ and $v^2=v_\parallel^2+2\Omega_i\mu$. The parallel derivative of B,

$$\boldsymbol{b}\cdot\nabla B = \frac{\varepsilon_tB_0}{q_0R_0}\left[\sin z+\sum_{l=L-1}^{l=L+1}\frac{\varepsilon_l}{\varepsilon_t}(l-Mq_0)\sin\left((l-Mq_0)z-M\alpha\right)\right], \tag{6}$$

is employed for the mirror force term.

The modified periodic condition is adopted at the radial boundaries of the flux tube domain [12]. Then, Φ is related to the electrostatic potential, ϕ, in the perpendicular wavenumber space, (k_x,k_y), such that $\Phi_{k_x,k_y}=J_0(k_\perp v_\perp/\Omega_i)\phi_{k_x,k_y}$ with $k_\perp^2=(k_x+\hat{s}zk_y)^2+k_y^2$ and the zeroth order Bessel function, J_0. The quasi-neutrality condition is used for calculation of ϕ_{k_x,k_y} (see Ref. [5] for more details). In the followings, we use the normalizations of $x/\rho_i\to x$, $tv_{ti}/L_n\to t$, $v/v_{ti}\to v$, $B/B_0\to B$, $e\phi L_n/T_i\rho_i\to\phi$, and $\delta f L_nv_{ti}^3/\rho_in_0\to\delta f$, where the thermal gyroradius is defined by $\rho_i=v_{ti}/\Omega_{i0}$ for $v_{ti}=\sqrt{T_i/m_i}$.

3. Gyrokinetic Theory and Simulation of Zonal Flows

Based on the gyrokinetic equation and the quasi-neutrality condition, we consider collisionless dynamics of the ITG-mode-driven zonal flows. When the initial perturbed ion gyrocenter distribution function takes the Maxwellian form, the response of the zonal-flow potential is given by

$$\phi_{\mathbf{k}_\perp}(t)=\mathscr{K}(t)\phi_{\mathbf{k}_\perp}(0), \qquad \mathscr{K}(t)=\mathscr{K}_{GAM}(t)[1-\mathscr{K}_L(t)]+\mathscr{K}_L(t) \tag{7}$$

where $\mathscr{K}(t)$ represents the response function (or kernel). Here, the short-time response $\mathscr{K}_{GAM}(t)$ is represented by $\mathscr{K}_{GAM}(t)=\cos(\omega_Gt)\exp(\gamma t)$, where ω_G and $|\gamma|=-\gamma$ denote the real frequency and the damping rate of GAM oscillations, respectively. Analytical expressions of ω_G and γ, which have been extended so as to take account of the finite-orbit-width (FOW) effects, are found in Refs. [15] and [6, 7] for tokamaks and helical systems, respectively. Global drift kinetic simulations of the GAM oscillation in helical systems are also done by Satake et al., and are compared with the theoretical analysis [16]. The long-time response function $\mathscr{K}_L(t)$ gives the normalized amplitude of the residual zonal flow in the limit of $t\to+\infty$. For tokamaks, $\mathscr{K}_L=1/(1+1.6\,q^2/\varepsilon^{1/2})$. The time-dependent $\mathscr{K}_L(t)$ for helical systems is given by

$$\mathscr{K}_L=\frac{1-(2/\pi)\langle(2\varepsilon_H)^{1/2}\{1-g_{i1}(t,\theta)\}\rangle}{1+G+\mathscr{E}(t)/\left(n_0\langle k_\perp^2a_i^2\rangle\right)} \tag{8}$$

(see Ref. [6, 7] for further details).

Analytical predictions about geometrical effects on the GAM dispersion relation, the residual zonal flows and the velocity-space structure of the distribution function in helical systems

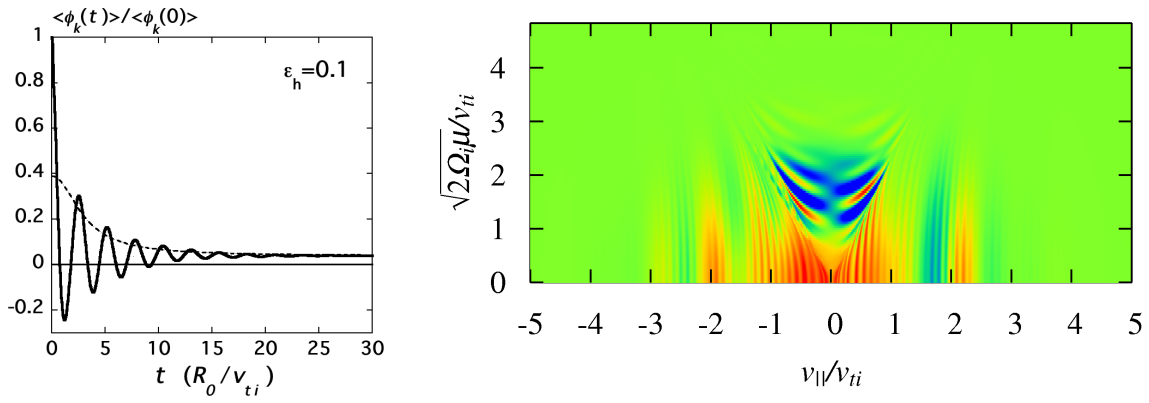

FIG. 1: (Left) Time-evolutions of the zonal-flow potential obtained by the GKV simulation for a helical system (solid) and the long-time response kernel derived from the gyrokinetic theory (dashed). A single helicity configuration with $L = 2$ and $M = 10$ is considered, such that $\varepsilon_h \equiv \varepsilon_L = 0.1$ and $\varepsilon_{L-1} = \varepsilon_{L+1} = 0$, where $q_0 = 1.5$ and $k_x\rho_i = 0.131$. (Right) Velocity-space structure of the ion distribution function in the velocity space during the collisionless damping of the zonal flow in a helical system with $L = 2$ and $M = 10$ at $\theta = 8\pi/13$ and $t = 6.23(R_0/v_{ti})$.

are compared with the GKV simulation results. Results of the GKV simulations of the collisionless zonal flow damping in helical systems are shown in Fig.1, where the initial potential given by the Maxwellian distribution with the poloidal and toroidal mode numbers, $m = n = 0$, is Landau-damped and then reaches a finite constant amplitude. The period numbers of the helical field in the poloidal and toroidal directions are $L = 2$ and $M = 10$, respectively. We used $q_0 = 1.5$ and $k_x\rho_i = 0.131$. The dashed line in the left panel of Fig.1 indicates the theoretically-obtained response kernel $\mathscr{K}_L(t)$ describing the long-time behavior of the zonal flow potential. The amplitude of the flux-surface-averaged potential, $\langle\phi_{\mathbf{k}}(t)\rangle$, oscillating with the GAM frequency, asymptotically approaches the residual level predicted by our theory. The GAM damping rate is enhanced by the FOW effect and the helical ripples, both of which produce lower parallel phase velocity components of the GAM and accordingly a larger population of resonant ions than in the case of tokamaks with no orbit widths. Also, the frequency and the damping rate of the GAM oscillations observed in the GKV simulations are in good agreement with the GAM dispersion relation that is analytically derived from the short-time zonal-flow response kernel [7].

The radial drift motions of particles trapped in helical ripples, which are related to neoclassical transport in the weak collisional regime, influence the long-time behavior of the zonal flow. The right panel in Fig.1 shows a real part of the perturbed ion gyrocenter distribution function $\delta f_{i\mathbf{k}}/(e\phi_{\mathbf{k}}/T_i)$ (normalized) in the velocity space, $(v_\parallel, v_\perp)$, obtained by the GKV simulation. Structures of $\delta f_{i\mathbf{k}}$ with fine stripes along the $v_\perp$-direction are caused by ballistic motions of passing particles. A distinct hollow profile in the helical-ripple-trapped region colored by blue is produced by the radial drift motion, and its averaged profile shows a remarkable agreement with the analytical solution. Our theoretical analysis also suggests that a higher-level zonal-flow response than in the tokamak case with the same aspect ratio can be maintained for a long time by suppressing the radial drift velocity of the helical-ripple-trapped particles.

The analytically-derived distribution function associated with the zonal flow is also used to construct a new gyrofluid closure model [17] (different from the Beer-Hammett model [18]) for zonal-flows driven by the tokamak ITG turbulence. The gyrokinetic theory and the gyrofluid closure model are recently extended to zonal flows in the electron temperature gradient

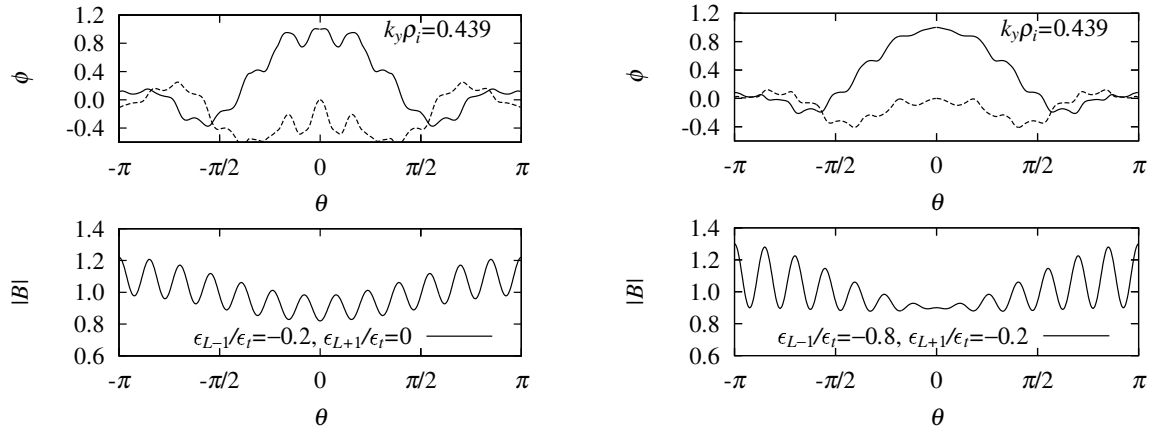

FIG. 2: Profiles of the electrostatic potential ϕ along the field line of the linear ITG mode (upper) and the magnetic field strength (lower) for the case (A) with $(\varepsilon_{L-1},\varepsilon_L,\varepsilon_{L+1})=\varepsilon_t(-0.2,1,-0)$ (left) and the case (B) with $(\varepsilon_{L-1},\varepsilon_L,\varepsilon_{L+1})=\varepsilon_t(-0.8,1,-0.2)$ (right). Real and imaginary parts of ϕ obtained by the GKV simulation for a helical system with $L=2$ and $M=10$ are, respectively, plotted by solid and dashed lines in the upper panels where $k_x=0$ and $k_y\rho_i=0.439$.

turbulence [17], and shows a remarkable agreement with the GKV simulations.

4. Simulation of ITG Turbulence in Helical Systems

It is expected from the above results on the zonal-flow dynamics that optimization of the three-dimensional magnetic configuration for reducing the neoclassical ripple transport can simultaneously enhance the residual zonal flows which lower the anomalous transport. In fact, it is observed in the Large Helical Device that not only neoclassical but also anomalous transport is reduced by the inward shift of the magnetic axis which decreases the radial ripple transport while magnetic-curvature-driven instabilities such as the toroidal ITG mode are more unstable [22]. Also, zonal flows are observed in the Compact Helical System [23]. Thus, we are encouraged to perform the GKV simulation of plasma turbulence in helical systems for further investigation into regulation of the anomalous transport by the zonal flow.

For this purpose, we have first carried out the GKV simulation of the linear ITG instability in helical systems. The eigenfunctions of the ITG mode in helical systems with $L=2$, $M=10$, and $\varepsilon_t=0.1$ are obtained by means of a linearized version of the GKV code, and are shown in upper panels of Fig.2. The magnetic field strength $|B|$ for the standard and inward-shifted configurations is modeled by Eq.(6) with $(\varepsilon_{L-1},\varepsilon_L,\varepsilon_{L+1})=\varepsilon_t(-0.2,1,0)$ and $(\varepsilon_{L-1},\varepsilon_L,\varepsilon_{L+1})=\varepsilon_t(-0.8,1,-0.2)$, respectively. Hereafter, we refer to the two different parameter sets as cases (A) and (B), respectively. Profiles of $|B|$ (normalized) along the field line are also plotted in lower panels of Fig.2. Other parameters are summarized as follows; $R_0/L_n=10/3$, $\varepsilon_{00}=0$, $R_0\varepsilon'_{00}=0.25$, $\alpha=0$, $r_0/\rho_i=246$, $\hat{s}=-1$, $q_0=1.5$, $\eta_i=4$, $T_e/T_i=1$, and $\nu_{ii}=2\times10^{-3}v_{ti}/L_n$. The linear growth rates of the mode with $k_x=0$ and $k_y\rho_i=0.439$ are $\gamma=0.0883v_{ti}/L_n$ and $\gamma=0.145v_{ti}/L_n$ for the cases (A) and (B), respectively. The ITG instability is driven stronger in the case (A) than that in the case (B), while the nearly constant bottoms of $|B|$ in the latter case mean the lower radial drift of deeply trapped particles in helical ripples. The profiles of the eigenfunction $\phi_{\boldsymbol{k}}(\theta)$ are accompanied with oscillations associated with the helical ripples. The linear eigenfunction of $\phi_{\boldsymbol{k}}$ has smaller ripples as the instability is driven stronger, and tends to resemble the profile in the negative-shear tokamak case [24].

The nonlinear ITG turbulence simulation in helical systems are performed by utilizing the

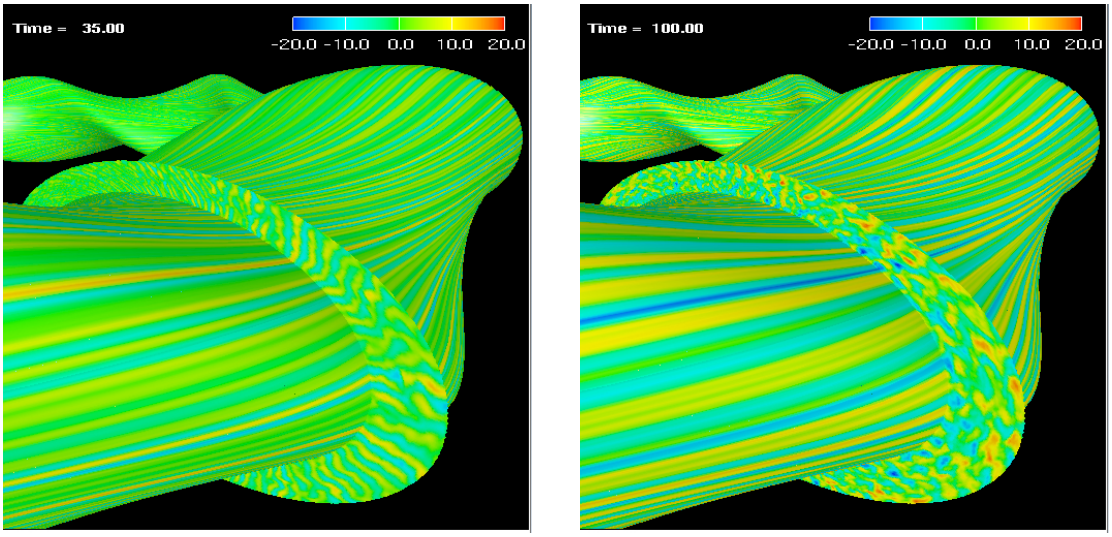

FIG. 3: Color contours of the perturbed electrostatic potential ϕ obtained from the nonlinear GKV simulation of the ITG turbulence in a helical system of $L = 2$ and $M = 10$ with $(\varepsilon_{L-1}, \varepsilon_L, \varepsilon_{L+1}) = \varepsilon_t(-0.2, 1, 0)$. The left and right panels are taken at $t = 35$ and $100L_n/v_{ti}$, respectively.

Earth Simulator [10]. The physical parameters are the same as those used in the linear ITG mode simulations. The simulation box size in the x and y directions are determined so that $\Delta q = -1/3$ and $N_\alpha = 6$, where Δq and N_α indicates a change in the safety factor across the radial width and the toroidal periodicity, respectively. Thus, the minimum absolute values of the wavenumbers are given by $k_{x,\min}\rho_i = 0.115$ and $k_{y,\min}\rho_i = 0.0366$. In the z- (θ-) coordinates along field lines, 512 grid points are used so as to accurately simulate the particle motions in the helical field. The simulation box in the velocity space is set to $-5v_{ti} \le v_\parallel \le 5v_{ti}$ and $0 \le \mu \le 12.5v_{ti}^2/\Omega_{i0}$, and is discretized by 128×48 numerical grid points of in the ($v_\parallel$, μ)-space. The high phase-space resolution enables us to carry out the GKV simulation that accurately satisfies the entropy balance. Even with $|L - Mq_0| = 13$ helical ripples along the field line in a range of $-\pi \le z \le \pi$, the entropy balance is satisfied with relatively small errors. In the case (A), the normalized error in the entropy balance is about 10% near the peak of the instability growth and decreases to $2 \sim 3$% in the saturation phase, while it is degraded to 30% in the case (B) due to the stronger instability.

Electrostatic potential perturbations obtained from the nonlinear GKV simulation for the case (A) are shown in Fig.3 where the color contours of ϕ at $t = 35$ and $100L_n/v_{ti}$ are mapped on the innermost flux surface and an elliptic poloidal cross-section. One can see that ballooning structures with radially elongated eddies found during the linear growth phase of the instability (left panel of Fig.3) are destroyed by zonal flows. Then, the ITG turbulence is saturated after $t = 80L_n/v_{ti}$ (right panel). Time-averaged power spectrum of the potential perturbations in the saturated turbulence peaks around $k_y\rho_i \approx 0.2$ or 0.3 (not shown in figures).

Time-histories of the ion heat transport coefficient, $\chi_i/(\rho_i^2 v_{ti}/L_n)$, are plotted in the left panel of Fig.4 for the cases (A) (solid) and (B) (dashed). After nonlinear oscillations during the saturation process of the instability growth, the turbulent transport reaches a statistically steady state. The transport coefficients averaged from $t = 80$ to $150L_n/v_{ti}$ are $\chi_i \sim 2.5\rho_i^2 v_{ti}/L_n$ and $\chi_i \sim 2.9\rho_i^2 v_{ti}/L_n$ in the cases (A) and (B), respectively. Since the ITG modes are more unstable in the case (B) as shown in Fig.2 [where the growth rates are 60% (or more) larger than those in case (A)], the peak value of χ_i becomes about 40% larger than that in the case (A). Nevertheless,

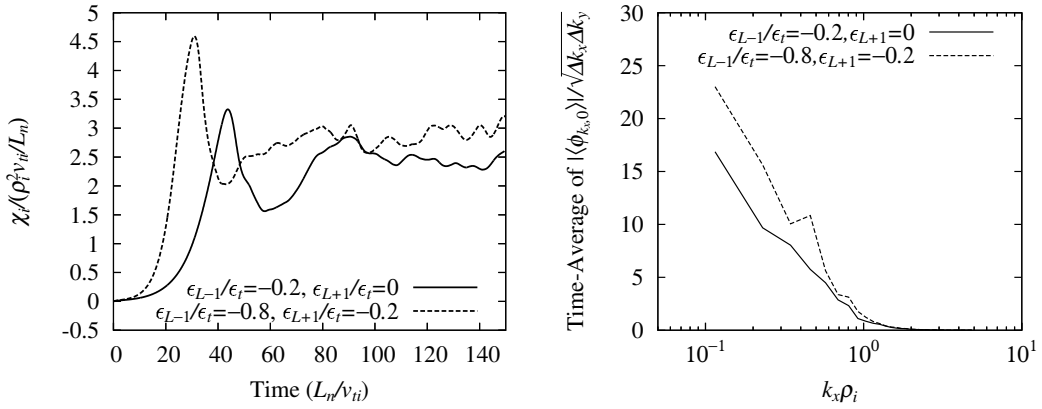

FIG. 4: Time-histories of the ion heat transport coefficient, χ_i, (left) and time-averaged spectrum of the zonal flow potential, $|\phi_{k_x,0}|$, (right) in the ITG turbulence in a helical system of $L = 2$ and $M = 10$ with $(\varepsilon_{L-1}, \varepsilon_L, \varepsilon_{L+1}) = \varepsilon_t(-0.2, 1, -0)$ [case (A), solid] and $(\varepsilon_{L-1}, \varepsilon_L, \varepsilon_{L+1}) = \varepsilon_t(-0.8, 1, -0.2)$ [case (B), dashed].

the time-averaged value of χ_i after $t = 80$ in the case (B) is only 16% higher than that in the case (A), and the temporal values of χ_i at $t = 90L_n/v_{ti}$ are comparable between the two cases. The effective transport suppression in the case (B) is attributed to the stronger zonal-flow generation as shown in the right panel of Fig.4. The time-averaged spectrum of $|\phi_{k_x,0}|$ in the case (B) has about 1.5 times larger amplitude than that in the case (A), which is consistent with a fact that the zonal flow response function has larger values in case (B).

In addition, typical radial scale lengths of the zonal flow potential observed in the helical ITG simulations are shorter than those found in the tokamak ITG case for the Cyclone DIII-D base case parameters [10]. Correspondingly, the zonal flow potential spectrum in the k_x-space has relatively smaller amplitude on the low k_x side. This tendency is expected from the k_x-dependence of the zonal flow response [6, 7]. Thus, the different zonal flow profiles found in the cases (A) and (B), as well as the difference between helical and tokamak systems, are correlated with their linear responses as predicted by the gyrokinetic theory [6, 7].

5. Summary

The gyrokinetic theory and simulations are applied to investigation of the zonal flow and the ITG turbulence in helical systems. The collisionless response of the zonal flow to given source terms is analytically derived and its validity is verified by the Eulerian gyrokinetic simulation code (GKV code) with very-high resolution of the phase space. The theoretical analysis predicts that a higher-level zonal-flow can be maintained by reducing the radial drift velocity of the helical-ripple-trapped ions. Then, the GKV code is extended for the nonlinear simulation of ITG turbulence in the two different helical geometries corresponding to the standard and inward-shifted configurations. In the latter case, the ITG mode is more unstable while the slower radial drift velocity of the helical-ripple-trapped particles. The ITG turbulent transport found in the GKV simulation for the inward-shifted configuration is more effectively suppressed by the zonal flow, and is reduced to the level which is comparable to the standard configuration case with linearly less unstable ITG modes.

Acknowledgments

The authors thank Dr. S. Ferrando i Margalet for performing simulations on zonal flows and

linear instabilities in helical systems, and also appreciate Dr. N. Nakajima, Dr. K. Ichiguchi, Dr. M. Yokoyama, Dr. S. Satake and Dr. H. Yamada for useful discussions on MHD equilibria, stability, GAM oscillations, and transport properties of helical plasmas. This work is supported in part by grants-in-aid of the Ministry of Education, Culture, Sports, Science and Technology (No. 16560727, 17360445, and 17·05373), and in part by the National Institute for Fusion Science (NIFS) Collaborative Research Program (NIFS05KKMT001, NIFS06KTAT038, NIFS06KDAD006, and NIFS06KNXN060). Numerical simulations are carried out by use of the Earth Simulator under the support by Japan Agency for Marine-Earth Science and Technology, and by use of the Plasma Simulator and the LHD numerical analysis system at National Institute for Fusion Science.

Reference

[1] HORTON, W., Rev. Mod. Phys. **71**, 735 (1999).
[2] DIAMOND, P.H., ITOH, S.-I., ITOH, K., HAHM, T.S., Plasma Phys. Control. Fusion **47**, R35 (2005); ITOH, K., et al., Phys. Plasmas **13**, 055502 (2006).
[3] ROSENBLUTH, R.M., HINTON, F.L., Phys. Rev. Lett. **80**, 724 (1998).
[4] WINSOR, N., JOHNSON, J.L., DAWSON, J.J., Phys. Plasmas **11**, 2448 (1968).
[5] WATANABE, T.-H., SUGAMA, H., Nucl. Fusion **46**, 24 (2006).
[6] SUGAMA, H, Watanabe, T.-H., Phys. Rev. Lett. **94**,115001 (2005).
[7] SUGAMA, H, Watanabe, T.-H., Phys. Plasmas **13**, 012501 (2006).
[8] KROMMES, J.A., HU, G., Phys. Plasmas **1**, 3211 (1994).
[9] SUGAMA, H., OKAMOTO, M., HORTON, W., WAKATANI, M., Phys. Plasmas **3**, 2379 (1996).
[10] WATANABE, T.-H., SUGAMA, H., FERRANDO I MARGALET, S., *"Gyrokinetic-Vlasov simulations of the ion temperature gradient turbulence in tokamak and helical systems"*, Proc. Joint Varenna-Lausanne Int. Workshop on Theory of Fusion Plasmas, Varenna, 2006 (American Institute of Physics, in press).
[11] FRIEMAN, E.A, CHEN, L., Phys. Fluids **25**, 502 (1982).
[12] BEER, M.A., COWLEY, S.C., HAMMETT, G.W., Phys. Plasmas **2**, 2687 (1995)
[13] SUGAMA, H., WATANABE, T.-H., Phys. Plasmas **11**, 3068 (2004).
[14] KURODA, T. et al., J. Phys. Soc. Jpn. **69**, 2485 (2000).
[15] SUGAMA, H., WATANABE, T.-H., *"Collisionless damping of geodesic acoustic modes"*, to be published in J. Plasma Phys (2006).
[16] SATAKE, S., et al., Nucl. Fusion **45**, 1362 (2005).
[17] SUGAMA, H., WATANABE, T.-H., FERRANDO I MARGALET, S., *"Gyrokinetic and gyrofluid models for zonal flow dynamics in ion and electron temperature gradient turbulence"*, Proc. Joint Varenna-Lausanne Int. Workshop on Theory of Fusion Plasmas, Varenna, 2006 (American Institute of Physics, in press).
[18] BEER, M.A., HAMMETT, G.W., Proc. Joint Varenna-Lausanne Int. Workshop on Theory of Fusion Plasmas, Varenna, 1998, edited by J. W. Connor, *et al*. (Societa Italiana de Fisca, Bologna, Italy, 1999) p.19.
[19] SUGAMA, H., WATANABE, T.-H., HORTON, W., Phys. Plasmas **8**, 2617 (2001).
[20] WATANABE, T.-H., SUGAMA, H., Phys. Plasmas **9**, 3659 (2002).
[21] WATANABE, T.-H., SUGAMA, H., Phys. Plasmas **11**, 1476 (2004).
[22] YAMADA, H., et al., Plasma Phys. Control. Fusion **43**, A55 (2001).
[23] FUJISAWA, A., et al., Phys. Rev. Lett. **93**, 165002 (2004).
[24] KURODA, T. et al., J. Phys. Soc. Jpn. **70**, 2235 (2001).